



OPEN A quantitative multi-parameter mapping protocol standardized for clinical research in multiple sclerosis

Henri Trang^{1,2,10}, Tim J. Hartung^{3,10}, Qianlan Chen¹, Stefan Hetzer⁴, Claudia Chien^{1,5,6}, Pia S. Sperber^{1,2,6}, Tanja Schmitz-Hübsch^{1,2,6}, Susanna Asseyer^{1,2,3,6}, Rebekka Rust^{1,6,7}, Darius Mewes^{1,8}, Lina Anderhalten^{1,2,6}, Michael Sy⁹, Alexander U. Brandt^{1,9}, Carsten Finke³✉ & Friedemann Paul^{1,2,3,6}✉

Quantitative magnetic resonance imaging (qMRI) involves mapping microstructure in standardized units sensitive to histological properties and supplements conventional MRI, which relies on contrast weighted images where intensities have no biophysical meaning. While measuring tissue properties such as myelin, iron or water content is desired in a disease context, qMRI changes may typically reflect mixed influences from aging or pre-clinical degeneration. We used a fast multi-parameter mapping (MPM) protocol for clinical routine at 3T to reconstruct whole-brain quantitative maps of magnetization transfer saturation (MT), proton density (PD), longitudinal (R1), and transverse relaxation rate (R2*) with 1.6 mm isotropic resolution. We report reference MPM values from a healthy population with age and gender distributions typical of multiple sclerosis in whole brain white matter (WM), T2-weighted WM hyperintensities, cortical grey matter and deep grey matter regions and present post-processing optimizations including integration of lesions and normalization of PD maps against cerebrospinal fluid (CSF) for standardized research in multiple sclerosis (MS) and potentially also in related disorders. PD maps were affected by WM abnormalities in MS using WM calibration. The results acknowledge the impact of non-linear age effects on MPM and suggest using CSF calibration for future clinical application in MS.

Keywords Quantitative MRI, Multi-parameter mapping, Neuroimaging, Multiple sclerosis, Aging, Proton density

Quantitative magnetic resonance imaging involves mapping microstructure in standardized physical units containing information about the local tissue environment surrounding the protons, thereby enhancing comparability in time and space. Quantitative maps supplement conventional MRI, which relies on contrast weighted images where intensities have no biophysical meaning, in providing insight into biologically meaningful microstructural properties of the central nervous system at the mesoscopic scale^{1,2}. Research in quantitative relaxometry and magnetization transfer imaging has shown strong reproducibility and sensitivity, exhibiting

¹Experimental and Clinical Research Center, a Cooperation Between Max Delbrück Center for Molecular Medicine in the Helmholtz Association, Charité – Universitätsmedizin Berlin, Geschäftsführung, Charitéplatz 1, 10117 Berlin, Germany. ²Max Delbrück Center for Molecular Medicine in the Helmholtz Association (MDC), Berlin, Germany. ³Department of Neurology and Experimental Neurology, Charité – Universitätsmedizin Berlin, Corporate Member of Freie Universität Berlin and Humboldt-Universität zu Berlin, Augustenburger Platz 1, 13353 Berlin, Germany. ⁴Berlin Center for Advanced Neuroimaging, Charité – Universitätsmedizin Berlin, Corporate Member of Freie Universität Berlin, Humboldt-Universität zu Berlin, and Berlin Institute of Health, Berlin, Germany. ⁵Department of Psychiatry and Neurosciences, Charité – Universitätsmedizin Berlin, Corporate Member of Freie Universität Berlin and Humboldt-Universität zu Berlin, and Berlin Institute of Health, Berlin, Germany. ⁶NCRC – Neuroscience Clinical Research Center, Charité – Universitätsmedizin Berlin, Berlin, Germany. ⁷Institut Für Med. Immunologie, Immundefektambulanz, Charité – Universitätsmedizin Berlin, Berlin, Germany. ⁸Berlin Institute of Health at Charité – Universitätsmedizin Berlin, Biomedical Innovation Academy, Berlin, Germany. ⁹Department of Neurology, University of California Irvine, 208 Sprague Hall, Mail Code 4032, Irvine, CA 92697, USA. ¹⁰These authors contributed equally: Henri Trang and Tim J. Hartung. ✉email: carsten.finke@charite.de; friedemann.paul@charite.de

a robust correlation with histological measurements and accepted metrics related to water³, myelin⁴, and iron content⁵.

Standardized scanning protocols at 3T and tools to reconstruct parametric maps demonstrating multi-center reproducibility are readily available^{6,7} such as the time-efficient multi-parameter mapping (MPM) protocol⁶ consisting of 3D multi-echo fast low angle shot (FLASH) acquisitions. It allows for estimation of quantitative maps of proton density (PD), magnetization transfer saturation (MT), longitudinal relaxation rate ($R1 = 1/T1$), and effective transverse relaxation rate ($R2^* = 1/T2^*$) facilitated by the open-source 'hMRI toolbox'⁸, which includes spatial processing tailored for voxel-wise statistical analysis of quantitative cerebral MRI data.

Several studies have collected quantitative relaxometry, MT and PD maps of healthy brain tissue using the MPM protocol to obtain normative reference values^{7,9}. These studies highlighted the influence of normal aging on brain microstructure in previous quantitative MRI studies^{10,11}.

This study aimed to optimize the post-processing of a previously described MPM protocol based on standard manufacturer sequences with 1.6 mm isotropic voxel resolution¹² for disease-related research into autoimmune neuroinflammatory diseases with affection of white matter such as multiple sclerosis (MS). MS is an immune-mediated inflammatory disease of the central nervous system shown to predominantly affect women, given a markedly high female to male ratio (~3:1)¹³. In a large healthy cohort with a gender distribution typical of neuroimmunology studies, we established reference values of MT, R1, PD and R2* in white matter (WM), T2-weighted (T2w) WM hyperintensities (WMH), cortical grey matter (CGM) and deep grey matter (DGM) regions. We compared WM and T2w WM hyperintensities values across MS patients and healthy controls. We standardized PD maps using reference values for water in cerebrospinal fluid (CSF) of the lateral ventricles¹⁴ and compared them to maps scaled to 69% in WM to highlight the impact of focal and diffuse white matter damage between MS patients and healthy controls. We further evaluated MPM-derived parameters and their associations with age and sex to inform future studies that may require strategies to correct for confounding effects of these factors when using MPM in clinical research.

Materials and methods

Subjects

Informed consent

The analysis was performed as part of two ongoing prospective observational studies BERLimmun¹⁵ (Berlin Registry of Neuroimmunological Entities, focusing on the course of neuroimmunological diseases, DRKS00026761), and CAMINO¹⁶ (study on cognition and MRI changes in patients with post-COVID syndrome), as well as another observational neuroimmunology study ViMS¹⁷ (examination of visual parameters in MS for the creation of a neuro-ophthalmologic register), approved by the institutional ethics committee of our institution (EA1/362/20, EA2/007/21, EA1/182/10 and EA1/163/12) and conducted in accordance with the Declaration of Helsinki in its applicable version for the conduction of the study. All participants gave written informed consent.

Study population

Demographics are summarized in Table 1. From April 2015 to September 2022, we pooled healthy participants recruited from the 3 previous separate registries. For the control group, participants without history of neurological or psychiatric disorders (and without previous COVID-19 infection for the CAMINO cohort) were recruited in Germany. Additional inclusion criteria were the following: self-declared healthy, older than 18 years of age, an active health insurance, competent to give written informed consent. Exclusion criteria consisted of

	MS	HC
Number of subjects [n]	27	77
Age [years], mean \pm SD	50 \pm 9.9	42.1 \pm 14.1
Total age range [years]	26–65	20–75
Age range for women [years]	26–65	20–75
Age range for men [years]	44–60	22–68
Female/male [n] (%female)	18F/9 M (67%)	60F/17 M (77.9%)
Disease course, [n]	RRMS n = 22 SPMS n = 5	NA
Number of subjects with cerebral WM lesions with a volume above 0.2 mL [n] (percentage)	27 (100%)	20 (26%)
Number of T2w WM hyperintensities, mean \pm SD	86.8 \pm 53.7	41.9 \pm 46.6
T2w hyperintensities volume [mL], mean \pm SD	21.5 \pm 12.2	1.39 \pm 1.63
EDSS, median (IQR)	3.0 (2)	NA
Disease duration (since symptom onset) [years], median (IQR)	15.9 (13.2)	NA

Table 1. Demographics and clinical characteristics of the participants. MS patients were diagnosed as RRMS according to 2017 revised McDonald criteria¹⁸ and as SPMS according to Lublin et al.⁵⁸. HC, healthy controls; F, female; M, male; WM, white matter; SD, standard deviation; IQR, interquartile range; RRMS, relapse-remitting multiple sclerosis; SPMS, secondary progressive multiple sclerosis; EDSS, Expanded Disability Status Scale.

contraindication to MRI investigation at inclusion, pregnancy, disease hindering the conduct of the study or inability to cooperate. Initially, we collected scans from 78 healthy participants. We excluded one participant from analyses because scans were of poor image quality. In total 77 healthy controls, 60 (77.9%) women and 17 (22.1%) men, with age ranging from 20 to 75 years, with a mean [\pm standard deviation (SD)] of 42.1 ± 14.1 years, were included (14 from BERLimmun, 14 from ViMS, 49 from CAMINO). Additionally, 27 patients diagnosed with MS (18 women (67%), mean age 50 ± 9.9 years) were included from the ViMS study according to the revised McDonald diagnosis criteria¹⁸.

MRI

Acquisition

MRI scans were acquired on a single 3T MR scanner (Magnetom Prisma, Siemens Healthineers, Erlangen, Germany) using a 64-channel receive radiofrequency (RF) head-neck coil covering brain and cervical spinal cord. To maintain reproducibility across participants and time points, the acquisition protocol, and participant positioning remained identical to that detailed in a prior study, aside from updating the head coil¹². Briefly, the MPM sequence is 7 min in length, 1.6 mm isotropic resolution with three distinct 3D multi-echo fast low-angle shot (FLASH) gradient-echo acquisitions. For post-acquisition bias-field correction, a radiofrequency (RF) transmit (B1+) map was acquired during each session with an isotropic resolution of 4 mm from spin-echo/stimulated echo acquisitions utilizing a standard vendor sequence⁷. MT-weighting was achieved by applying an off-resonance Gaussian pulse (500°, 10 ms, 1200 Hz off-resonance, 192 Hz bandwidth) prior to non-selective excitation. In addition, the BERLimmun scan protocol included a structural T1-weighted (T1w) scan (3D MPRAGE, TR=1900 ms, TE=2.55 ms, TI=900 ms, 0.8 mm isotropic resolution) and T2w fluid-attenuated inversion recovery (3D FLAIR, TR=6000 ms, TE=388 ms, TI=2100 ms, 0.8 mm isotropic resolution). The CAMINO scan protocol included a 3D-MPRAGE (1 mm isotropic resolution, TR=1900 ms, TE=2.22 ms, TI=2100 ms).

Quantitative map reconstruction

We generated quantitative PD, MT, R1, and R2* maps utilizing MATLAB (MathWorks) with the hMRI toolbox (RRID:SCR_017682)⁸ implemented within SPM12 (<http://www.fil.ion.ucl.ac.uk/spm/software/spm12/>, RRID:SCR_007037). These maps were reconstructed given the PD-weighted (PDw), MT-weighted (MTw), and T1w echoes acquired through FLASH acquisitions and corrected for transmit and receive field inhomogeneities¹⁹. Correction of Gibbs ringing artifacts²⁰ was performed prior to reconstruction of the quantitative maps, consisting in the removal of oscillatory patterns situated around tissue borders from all six echoes of the raw images (PDw, MTw, T1w). Motion degradation index for each of the raw averaged echo images (PDw, MTw, T1w) were obtained from the toolbox to identify scans with motion artifacts²¹. Correlation of motion degradation index with age was assessed to evaluate the impact of motion on R2* variability with age (Sup. Fig. S1). Finally, given the use of an off-saturation MT pulse with a flip angle of 500°, we linearly rescaled MT maps to harmonize values for comparison to literature values obtained with a 220° flip angle, as recent evidence showed that a linear rescaling to harmonize MT maps across manufacturers effectively reduced the inter-site bias⁷.

Post-processing

T1-MPRAGE and T2-FLAIR images underwent bias-field correction using non-parametric non-uniform intensity normalization (RRID:SCR_004757)²² and were subsequently reoriented to the Montreal Neurological Institute (MNI) standard reference space for further lesion delineation using FSL FLIRT (<http://www.fmrib.ox.ac.uk/fsl>, RRID:SCR_024922).

Segmentation

Two expert MRI technicians (15–17 years of experience) performed manual segmentation using ITK-SNAP (available at www.itksnap.org) of T2w hyperintense brain lesions on FLAIR images linearly co-registered to MPRAGE images²³. We subsequently refer to our segmentations as WM lesions (WML), rather than the general T2w-hyperintensities. We only included lesion masks with a WML mean volume above a pragmatic cutoff of 0.20 mL, corresponding to a Fazekas visual rating score of 1^{24,25}. Generation of a brain mask and tissue segmentation of T1-MPRAGE images to obtain WM, CGM and DGM masks were achieved via FastSurfer²⁶. Lesion-filled WM masks were obtained by subtracting lesions from WM masks. Additionally, for each mask, voxels with T1 values higher than 4 s within the tissue masks were removed for further correction of partial volume effect²⁷. All masks and structural images were then linearly co-registered via FSL FLIRT to native space using the T1w image as reference. Median parameter values were extracted from WM, CGM and several atlas-defined (Desikan-Killiany, DK)²⁸ deep grey matter structures (thalamus, caudate nucleus, putamen, globus pallidus, hippocampus, amygdala, and nucleus accumbens) for each participant with both hemispheres summed.

PD calibration

The PD map output from the hMRI toolbox was corrected for R2* by extrapolating the signal at TE=0 ms and was originally calibrated as 69% water content in the WM⁸. To demonstrate bias resulting from WM abnormalities in MS patients, PD maps calibrated using a whole WM mask and a lesion-filled WM mask were compared respectively in the whole WM region (including WML) and the normal appearing WM region free of WML (NAWM). Subsequently, reconstructed PD maps from the hMRI toolbox were recalibrated as pure water (100% reference) based on the median CSF signal in the lateral ventricles²⁷, using a mask from the Harvard Oxford template distributed with FSL (Functional MRI of the Brain Software Library, <http://www.fmrib.ox.ac.uk/fsl/>, RRID:SCR_002823) warped into subject native space. To reduce partial volume effects, lateral ventricles masks were eroded by 1 voxel then corrected by multiplying them with a CSF tissue mask obtained from the respective

tissue probability map (threshold of 0.9). Finally, we excluded voxels with T1 values lower than 4s to obtain only voxels with pure water in CSF, based on the quantitative R1 map output from the reconstruction toolbox. To account for a potential bias introduced by CSF volume or T1 variability in CSF, we compared our method to a calibration selecting only the 100 voxels with the shortest T1 times above the 4s cutoff, therefore obtaining a mask with the same volume across participants over voxels with a small range of T1 above 4s. We calculated coefficients of variation (CoV) of the scaling factor, which is the multiplication factor obtained to scale each individual PD map by dividing 100% by its respective median in CSF. The corresponding mathematical formula is given by the following equation :

$$\text{Normalized PD} = \frac{PD * 100}{\text{median}(PD|T1 > 4s, CSF)} = PD * \text{scaling factor}$$

Statistical analyses

Descriptive statistics

Histogram analysis of brain tissues was first done to assess distribution of the entire dataset of healthy controls in WM, WML, CGM and DGM (Sup. Fig. S2). Population age and sex distributions are shown in Sup. Fig. S3. To get a better representation of a healthy population cross-sectional data for each brain region of interest (ROI), all subsequent analyses were performed on data free from respective outliers outside the ROI-specific 2nd–98th percentile. Statistical analysis was conducted in R (R Core Team, <https://www.r-project.org>). Normality of data distribution was tested using a Shapiro–Wilk test (“rstatix” R package, RRID:SCR_021240). Median MPM metrics in each brain ROI were used for statistical analysis. Volume of the considered ROI was normalized by total intracranial volume to obtain an adjusted volume and account for intracranial volume differences between men and women. This volume will be referred to as normalized ROI volume. Differences between WM and WML across MS patients and healthy controls were assessed using ANOVA and linear regression models adjusted for age and sex followed by post-hoc Tukey tests (“emmeans” R package, RRID:SCR_018734). Additionally, in MS patients, using linear regression models adjusted for age and sex, we explored the association between MPM-derived measures and clinical disability measured by the expanded disability status scale²⁹ (EDSS, higher score means more neurological disability), disease duration or T2 lesion volume.

Sex differences

Interaction between sex and age was tested before excluding the former variable as a possible covariate for MPM-derived parameters. Analysis of sex on median MPM parameter in healthy controls showed no statistically significant difference between men and women, including normalized ROI volume as an additional covariate in the linear regression model. Therefore, all regression models were fitted non-stratified, i.e. by combining data from both men and women.

MPM age effects

For the assessment of the relationship between MPM-derived parameters and age, MS subjects were excluded. Linear and non-linear relationships between each MPM parameter and age were tested for every structure. P-values are adjusted for multiple comparisons using the Benjamini–Hochberg method. A polynomial regression model was built for each tissue parameter with age, adding normalized ROI volume and sex as covariables. Orthogonal polynomials were used to reduce multicollinearity effects of age predictors (e.g. covariance of age, age², age³). This was implemented in R using the “poly()” function from the “stats” package (RRID:SCR_025678). Non-linear volume dependency with age was further assessed by exploring the significance of the quadratic term.

Additionally, visual inspection of MPM-by-age scatterplots with LOESS-fitted trend lines indicated that a 1-knot linear spline model could best fit the age-related distribution. We selected a cutoff of 55 years (≥ 55) for the spline, which represented a split at approximately the 80th quantile. This is consistent with the upper age limit of most clinical drug trials in multiple sclerosis, as the confounding effect of vascular lesions and other comorbidities increases beyond this cut-off. Furthermore, diffusion tensor imaging studies revealed that age-related decline is more apparent in the fifth decade of life³⁰.

Permutation testing was conducted with 1000 iterations to assess statistical significance at two levels: (1) an overall test for the entire linear model, and (2) term-specific permutation tests for each predictor to assess the significance of individual terms. The F-statistic from the original model was calculated, and for each permutation, the age and sex values were independently shuffled. The F-statistic for the permuted model was then computed. The permutation *p*-value was determined by calculating the proportion of permuted F-statistics that were greater than or equal to the original F-statistic. For the term-specific tests, we selectively shuffled the values of age and sex independently in each iteration. The model was refitted to the permuted data, and the coefficients for each term were recorded. The empirical *p*-value for each term was calculated by determining the proportion of permuted coefficients whose absolute values were greater than or equal to the absolute value of the original estimate. Additionally, bootstrapping was done with 1000 resamples to estimate the stability and 95% confidence intervals of the model coefficients. The bootstrapping procedure involved resampling the dataset with replacement, fitting the linear model to each bootstrapped sample, and recording the coefficients.

Model selection

We compared the performance of linear, linear spline, quadratic, cubic and exponential models to choose the simplest best fitting model according to a likelihood ratio test in addition to Akaike information criterion (AIC) comparison. The simplest model was generally chosen when the likelihood ratio-test did not return a significant difference.

Results

PD calibration

We chose to standardize PD based on ventricular CSF (see Fig. 1 for an illustration of the pipeline), since calibration methods using lesion-filled WM masks and whole WM masks in 27 MS patients resulted in different PD values in NAWM and WM (Fig. 2a). In contrast, no difference was found between NAWM and WM in effective PD (without calibration) or when using CSF as reference (Fig. 2b and c).

Lateral ventricles masks had a median volume of 5685(7934) [median(IQR)] voxels or 23.3(32.5) mL. Exclusion of voxels with a T1 below 4s resulted in a median mask volume of 2683(4596) voxels or 10.99(18.82) mL. The average percentage of voxels remaining above this T1 threshold was 44.31% (mask voxel number ranging from 262 to 31,396) with a range of T1 times from 4 to 13.4 s. Median T1 across participants was 5.4 s in this CSF mask. CoV of the scaling factor using CSF were 1.51%, 0.74% and 2.38% for respective T1 thresholds at 3 s, 4 s and 5 s, compared to 37.79% for the calibration using WM. Using only the first 100 voxels with T1 > 4 s in the mask resulted in a CoV of the scaling factor of 2.20%. Normalized lateral ventricles volume was correlated with age and scaling factor for the calibration using CSF, as well as scaling factor with age. However, there was no association between PD in the lateral ventricles and age (Sup. Fig. S4). After normalization with the CSF signal, mean intra-subject CoV of PD was $5.2 \pm 0.33\%$ in WM, $8.26 \pm 0.58\%$ in CGM and $4.84 \pm 0.48\%$ in DGM. Intra-subject variability remained identical to the WM-based calibration due to the linear rescaling of effective PD. SD of PD across subjects were higher in WM (1.27 vs. 0.17), CGM (1.10 vs. 0.68) and DGM (1.19 vs. 0.69) with the normalization to CSF compared to calibration of PD against WM resulting in higher inter-subject CoV in WM (1.82% vs. 0.24%), in CGM (1.40% vs. 0.86%) and in DGM (1.54% vs. 0.88%).

Healthy cohort reference values

Table 2 presents descriptive statistics of MPM measurements in WM, WML, CGM, DGM, thalamus, hippocampus and CSF. Data for caudate nucleus, putamen, globus pallidus, amygdala, nucleus accumbens are

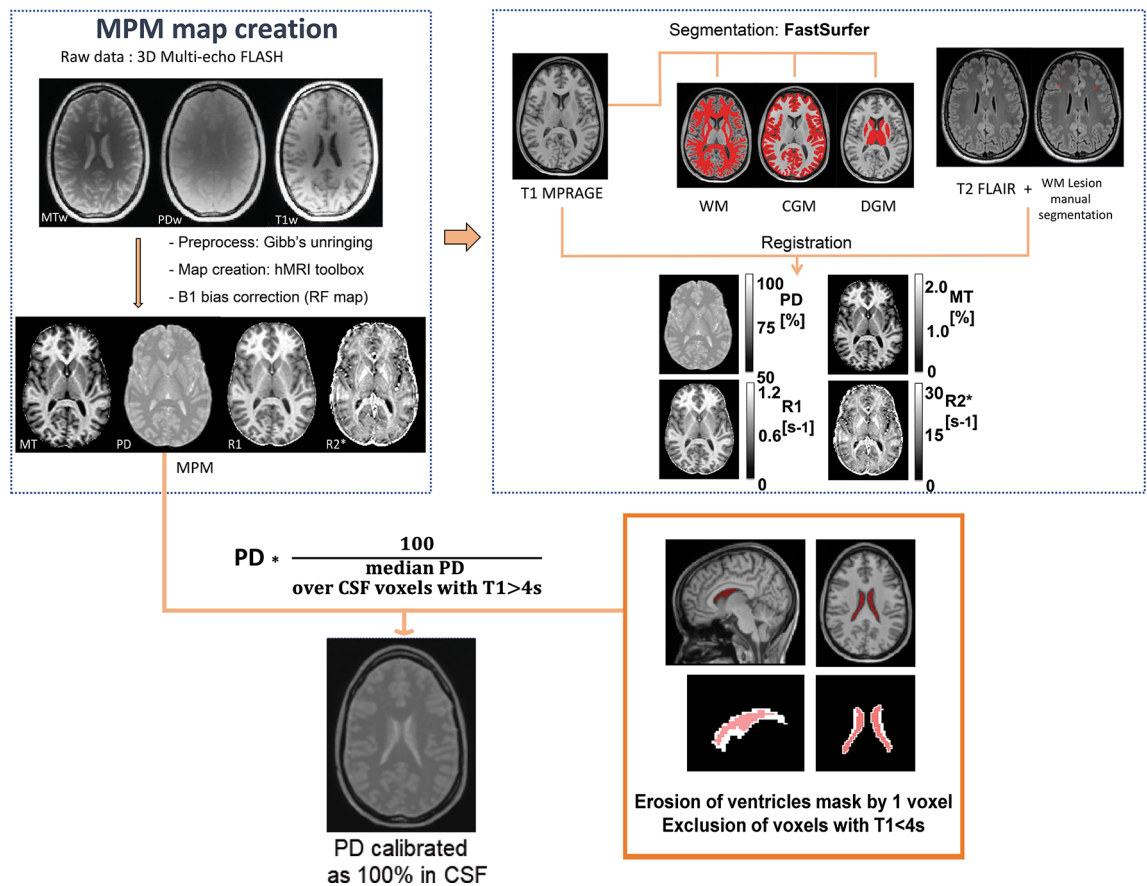


Fig. 1. Graphical representation of the MPM pipeline. Raw PDw, MTw, T1w echoes were corrected for Gibb's artifact before reconstruction with the hMRI toolbox. Receive field inhomogeneities were corrected using Unified Segmentation. T1-MPRAGE was segmented using Fastsurfer, a deep learning alternative to FreeSurfer, to obtain tissue masks for white matter (WM), cortical grey matter (CGM) and deep grey matter (DGM). White matter T2 hyperintensities were manually segmented from T2-FLAIR. All masks were then spatially registered to the quantitative maps. PD maps were calibrated as 100% in ventricular CSF. Voxels with T1 < 4s were excluded from the eroded lateral ventricles mask.

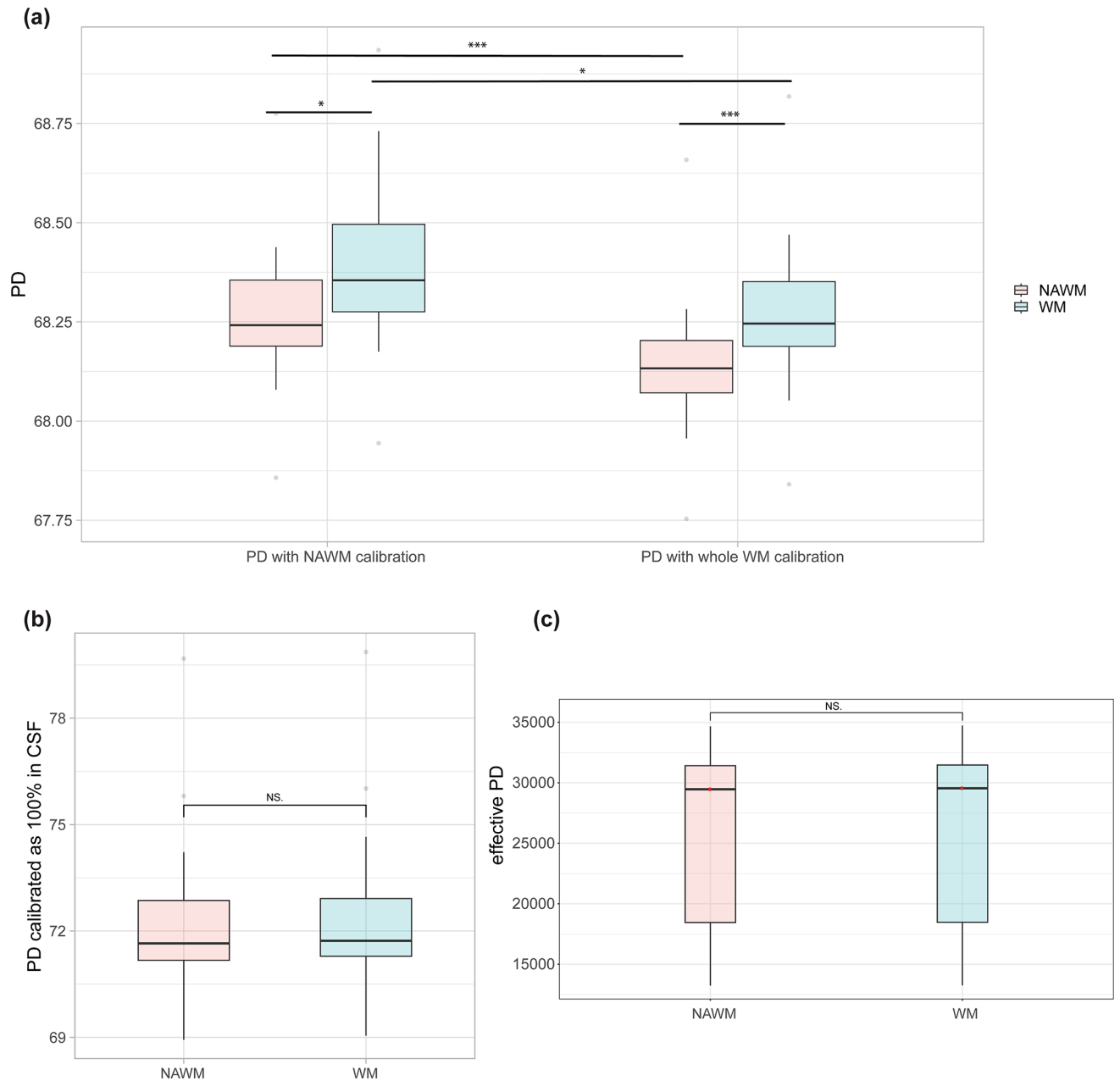


Fig. 2. (a) PD comparison in whole white matter (WM) and normal-appearing white matter (NAWM) of 27 MS patients between calibration methods using lesion-filled white matter mask (PD with NAWM calibration) and whole white matter mask (PD with whole WM calibration). Significance levels associated to asterisks: $p < 0.05$ (*), $p < 0.01$ (**), $p < 0.001$ (***). (b) Comparison of PD maps calibrated using CSF signal in normal appearing white matter (NAWM) and whole white matter (WM) regions of MS patients. Using CSF calibration, the mean difference between NAWM and WM is 0.1 p.u, which is of the same order of magnitude as in (a). Standard deviations are higher resulting in a higher inter-subject coefficient of variation. (c) Comparison of non-calibrated PD maps in normal appearing white matter (NAWM) and whole white matter (WM) regions of MS patients.

presented in Sup. Tables S1, S2. Reported mean or median values across ROIs are in line with those reported in previous studies (Sup. Table S2).

Histograms (Fig. 3a) show clearly distinct peaks and normal distributions of MPM median values for WM, WML, CGM and DGM. Detailed distribution density of median parameter values in DGM structures is shown in Fig. 4a. The pallidum stands out among the deep grey matter structures with higher MT, R1 and R2* and lower PD (Fig. 4a). This is further illustrated in Fig. 4b displaying a brain slice sampled from each population averaged parameter map.

ROI	Parameter						
	WM	WML	CGM	DGM	Thalamus	Hippocampus	CSF
MT (%)							
Mean (SD)	1.55 (0.05)	1.24 (0.19)	0.85 (0.02)	1.05 (0.04)	1.17 (0.05)	0.83 (0.03)	0.023 (0.007)
Overall ROI SD	0.28	0.3	0.27	0.24	0.24	0.18	0.020
Median (IQR)	1.6 (0.06)	1.26 (0.27)	0.85 (0.03)	1.03 (0.04)	1.2 (0.07)	0.82 (0.03)	0.017 (0.008)
Intra-subject CoV (%)	18.16	25.23	31.40	22.77	20.23	21.41	89.25
Inter-subject CoV (%)	3.21	15.28	2.78	3.43	4.13	4.12	30.01
2nd–98th Percentile	1.42–1.64	0.91–1.57	0.8–0.89	0.97–1.12	1.07–1.26	0.75–0.89	0.01–0.05
Min–Max (of means)	1.4–1.64	0.87–1.62	0.79–0.89	0.95–1.12	1.04–1.26	0.73–0.91	0.01–0.05
PD (%)							
Mean (SD)	69.97 (1.27)	72.91 (2.94)	78.73 (1.10)	77.37 (1.19)	76.53 (1.20)	78.9 (1.27)	100.72 (0.33)
Overall ROI SD	3.64	4.63	6.5	3.75	4.11	3.24	4.55
Median (IQR)	69.08 (1.84)	72.8 (4.11)	78.81 (1.36)	77.76 (2.05)	76.61 (1.78)	79.14 (1.72)	100.14 (0.23)
Intra-subject CoV	5.20	6.41	8.26	4.84	5.38	4.11	4.52
Inter-subject CoV	1.82	4.03	1.40	1.54	1.57	1.60	0.33
2nd–98th Percentile	67.67–72.22	67.13–77.48	76.32–80.76	75–79.26	74.15–78.77	76.47–80.82	100.27–101.83
Min–Max	66.87–72.53	66.24–77.56	76.29–81.17	74.03–79.32	73.78–79.09	75.27–80.93	100.04–101.98
R1 (s ⁻¹)							
Mean (SD)	0.91 (0.03)	0.81 (0.08)	0.62 (0.01)	0.7 (0.02)	0.73 (0.02)	0.58 (0.02)	0.185 (0.005)
Overall ROI SD	0.12	0.13	0.1	0.11	0.09	0.07	0.016
Median (IQR)	0.92 (0.04)	0.82 (0.16)	0.61 (0.02)	0.7 (0.03)	0.73 (0.03)	0.57 (0.02)	0.186 (0.009)
Intra-subject CoV	13.62	16.64	16.34	15.59	12.84	11.25	8.71
Inter-subject CoV	2.91	9.29	2.07	2.90	3.41	2.96	2.61
2nd–98th Percentile	0.85–0.96	0.7–0.94	0.59–0.64	0.67–0.74	0.67–0.77	0.55–0.62	0.17–0.19
Min–Max	0.83–0.96	0.7–0.95	0.58–0.64	0.66–0.74	0.65–0.78	0.54–0.62	0.14–0.20
R2* (s ⁻¹)							
Mean (SD)	21.29 (0.56)	18.99 (4.11)	18.01 (0.59)	20.89 (1.07)	20.23 (0.97)	15.92 (0.78)	2.23 (0.67)
Overall ROI SD	4.23	5.48	9.19	6.44	3.57	3.9	2.06
Median (IQR)	21.06 (0.87)	18.24 (2.27)	16.8 (0.78)	20.24 (1.13)	20.37 (1.09)	15.61(0.84)	1.74 (0.52)
Intra-subject CoV	19.87	25.69	51.03	30.66	17.67	24.44	90.37
Inter-subject CoV	2.64	21.61	3.30	5.11	4.80	4.92	30.03
2nd–98th Percentile	20.4–22.23	15.58–29.6	16.96–18.96	19.06–23.32	18.4–22.28	14.63–17.71	1.39–5.16
Min–Max	20.11–22.32	15.44–34.94	16.78–19.02	18.68–24.12	18.27–22.61	14.44–18.97	1.32– 5.98
Volume (mL)							
Mean (SD)	182.15 (9.52)	1.39 (1.63)	199.85 (11.37)	15.61 (1.45)	5 (0.45)	1.05 (0.9)	18.17 (20.35)
Mean ICV (mL)			2890 (256.05)				

Table 2. Descriptive statistics for all MPM and volume measurements in white matter (WM), white matter lesions (WML), cortical grey matter (CGM), deep grey matter (DGM), thalamus, hippocampus and CSF. We averaged overall ROI SD (standard deviation across ROI voxels) and intra-subject coefficient of variation across participants. Min–Max represent minimum and maximum of mean ROI values across participants. CSF values were extracted from the lateral ventricles excluding voxels with T1 values lower than 4s. Please note that PD values are scaled to 100 p.u. normalized by the median CSF value. MT values have been linearly rescaled to reference values of a MT pulse of 220° for comparison purpose to literature. SD, standard deviation; IQR, interquartile range; CoV, coefficient of variation; ROI, region of interest; CSF, cerebrospinal fluid.

White matter lesions and white matter alterations

Fifty-two out of 77 healthy participants (67.5%) had at least one T2w WMH segmented as lesion (single lesion volume > 0.01 mL) and 20 (26%) participants (mean age 50.5 ± 14y, 6 (30% male)) had a mean WML volume above the pre-defined cutoff of 0.2 mL. Mean (SD) number of lesions was 41.9 (46.6) and mean WML volume was 1.39 (1.63) mL (Tables 1 and 2). MPM metrics and lesion volume scatterplots against age are shown in Sup. Fig. S5.

In healthy participants, compared to healthy WM, MPM values in WML were significantly reduced for MT ($t = -7.53$, 95% CI = [-0.43, -0.24], $p < 0.001$), R1 ($t = -5.83$, 95% CI = [-0.14, -0.07], $p < 0.001$) and R2* ($t = -8.05$, 95% CI = [-3.56, -2.09], $p < 0.001$) and significantly increased for PD ($t = 5.51$, 95% CI = [2.31, 5.12], $p < 0.001$). In addition, WML showed a substantially wider range of MPM values across all parameters, compared to healthy WM (Fig. 3).

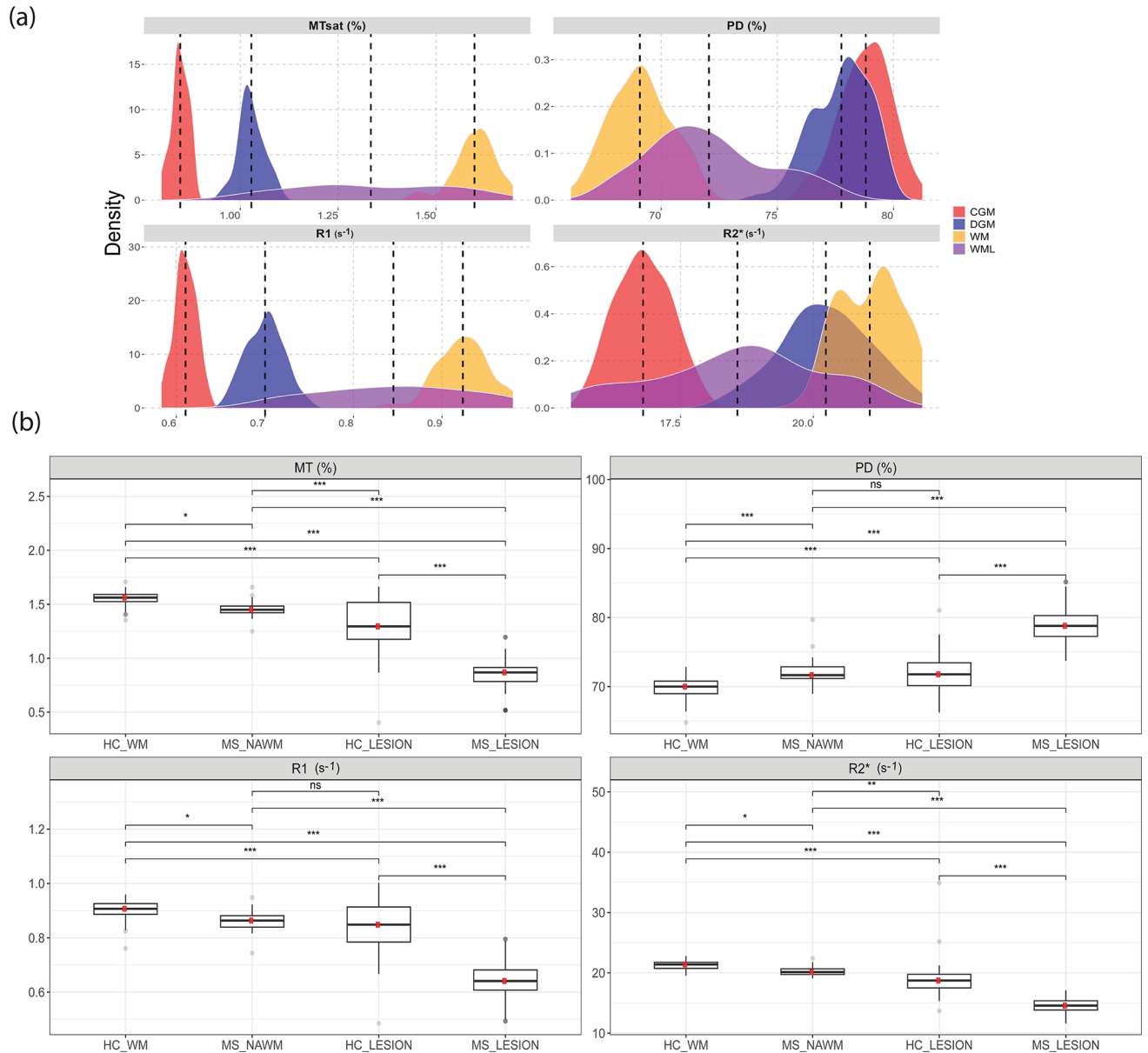


Fig. 3. (a) Histograms of median MPM values distributions across healthy participants in white matter (WM, yellow), white matter lesions (WML, purple), cortical grey matter (CGM, red), deep grey matter (DGM, blue). Dashed lines indicate respective median. For each tissue class except WML, outliers outside the 2–98th percentile were removed. WML only included median values of healthy participants with mean volume higher than 0.2 mL. (b) MPM comparison of white matter lesions in MS patients (MS_LESION) and HC T2w white matter hyperintensities (HC_LESION) against healthy white matter (HC_WM) of healthy controls and normal appearing white matter of MS patients (MS_NAWM, free of lesions). Significance levels associated to asterisks: $p < 0.05$ (*), $p < 0.01$ (**), $p < 0.001$ (***).

MS patients had a mean T2w WMH volume of 21.5 (12.2) mL ranging from 10.3 to 58.2 mL across patients and a mean number of lesions of 86.8 (53.7). MS-WML had increased PD and reduced MT, R1 and R2* compared to MS-NAWM, HC-WM and HC-WML (Fig. 3b).

In MS-WML and NAWM, we explored significant associations between MPM parameters and the following clinical variables: EDSS, disease duration and T2w WMH volume. In WML, we found a positive association between PD and EDSS ($\beta = 0.908$, 95% CI = [0.320, 1.495], $p = 0.004$) and negative associations between MT and EDSS ($\beta = -0.053$ [-0.083, -0.024], $p = 0.001$), and between R1 and EDSS ($\beta = -0.020$ [-0.035, -0.005], $p = 0.010$), while no statistically significant association to disease duration or T2 lesion volume across parameters was observed. In NAWM, MT ($\beta = -0.013$ [-0.023 to -0.003], $p = 0.011$) and PD ($\beta = 0.432$ [0.164, 0.699], $p = 0.002$) were associated with EDSS. MT ($\beta = -0.002$ [-0.004, -0.001], $p = 0.009$), PD ($\beta = 0.094$ [0.055, 0.134]), $p < 0.001$), R1 ($\beta = -0.0016$ [-0.0023, -0.0009]), $p < 0.001$) and R2* ($\beta = 0.0197$ [0.0026, 0.0368], $p = 0.024$) were associated with disease duration. MT ($\beta = -0.003$ [-0.004, -0.002], $p < 0.001$), PD ($\beta = 0.112$

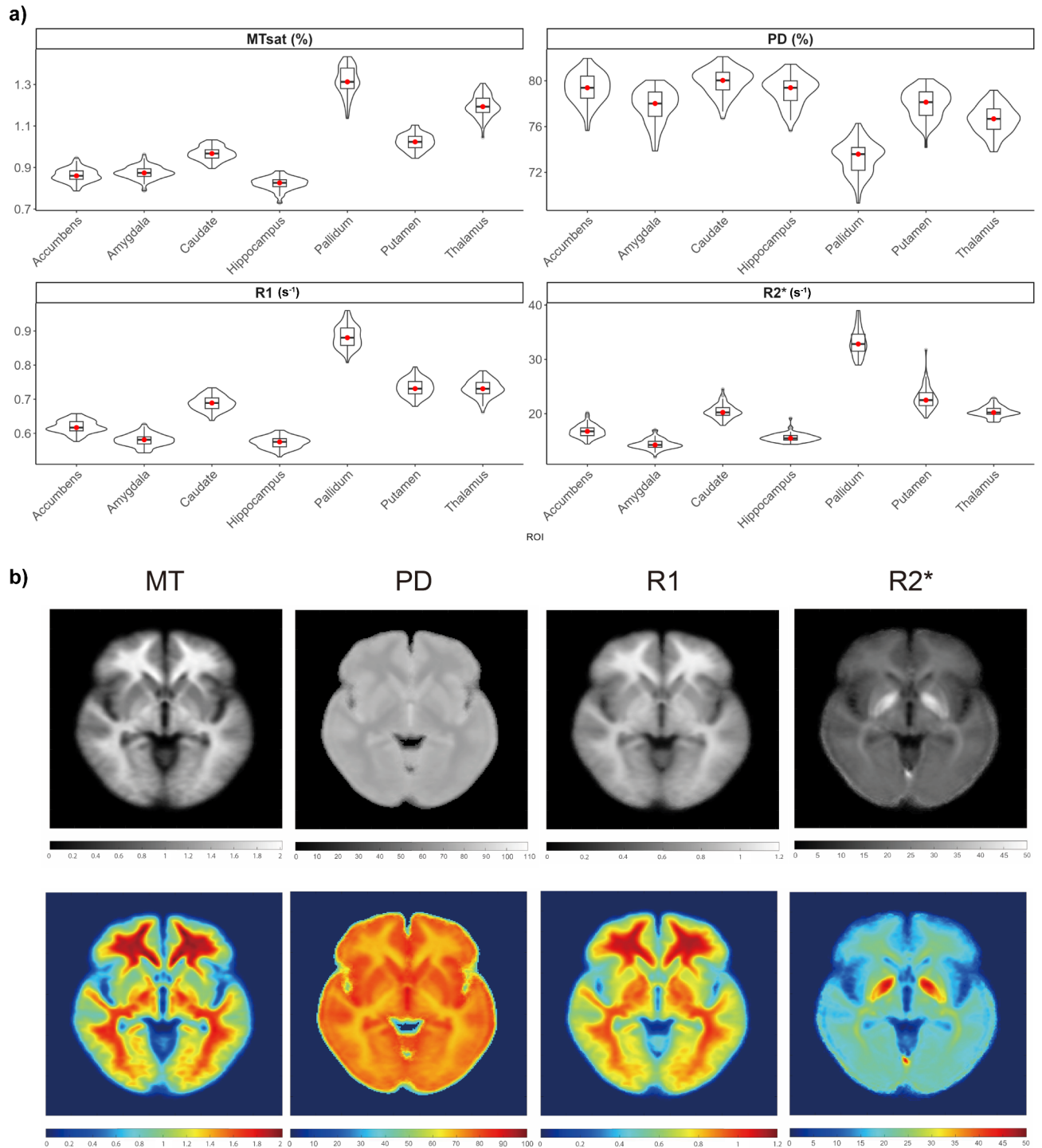


Fig. 4. (a) Boxplots and density distribution comparison of median MT, PD, R1 and R2* values in thalamus, caudate, globus pallidus (Pallidum), putamen, amygdala, hippocampus, nucleus accumbens (Accumbens). (b) Greyscale and RGB-colored slice examples of population averaged quantitative maps showing globus pallidus caudate putamen and thalamus. In particular, the globus pallidus shows higher R2*, R1, MT and lower PD values.

[0.088, 0.136], $p < 0.001$) and R1 ($\beta = -0.0017$ [-0.0021, -0.0012], $p < 0.001$) were associated with T2w WMH volume.

MPM age related changes

As part of our objective to explore the impact of brain aging on the quantitative maps, Table 3 compiles effect sizes from the regression models, including 95% confidence intervals. Only models revealing a significant

association between parameter and age in WM, CGM, DGM, thalamus and hippocampus are presented in Table 3 and outcomes of model selection are summarized in Sup. Fig. S6. For data visualization, scatterplots with the trajectory of the curve fitting in the various ROIs are attached in Fig. 5 and Sup. Fig. S7.

Regression of MT, R1 and R2* showed a non-linear association with age in the quadratic term in both WM and CGM. In the thalamus, fitting MT and R1 with a quadratic function against age showed significant association, both described by a slow increase from 20 to 40y followed by a decline after 50y. In the hippocampus only R1 presented a quadratic evolution with age indicating a slow increase from 20 to 50y followed by a decline after 60y.

In WM, a linear spline performed better than a quadratic fit in explaining changes in MT and R2* with age. Summarizing the results of the model selection in WM (Table 3), MT showed an average decrease of $-0.154\%/year$ ($p < 0.001$) after 55y, R2* a decrease of $-0.648s^{-1}/year$ ($p < 0.001$) after 55y and PD increased linearly by $0.033\%/year$ ($p = 0.002$). R1 revealed a quadratic association with age ($p = 0.005$) with a slow increase over 20–40y followed by a decline after 50y. Remarkably, there was no age association in both MT and R2* in WM between 20 and 55y.

In CGM, selected models were quadratic for MT, R1 and R2* and linear for PD. In the thalamus, a quadratic fit was selected for MT and R1 and in the hippocampus R1 also showed a quadratic trajectory with age.

Finally, there was no non-linear volume dependency with age across ROIs when testing the quadratic term, although correlation was present (Sup. Table S3).

Discussion

In this study we present an acquisition and post-processing protocol for a fast quantitative multi-parameter mapping of the brain with inclusion of T2w white matter hyperintensities and calibration of proton density using CSF. We standardize the reconstructed quantitative maps for future clinical application in autoimmune neuroinflammatory diseases such as multiple sclerosis and recommend calibrating PD maps as pure water in CSF to avoid bias introduced by pathology. We report reference MPM brain data for 77 healthy subjects of Caucasian ethnicity aged between 20 and 75 years and discuss age-dependence of the MPM parameters.

PD calibration

PD maps using the standard approach from the hMRI toolbox reconstruction are calibrated to 69% in WM which may lead to an underestimation of its reported variability⁷. In addition, pathologic changes of PD in WM may not be reflected, especially when considering its possible use in diseases with WM abnormalities, e.g. multiple sclerosis. Using CSF-based calibration avoids these problems, as CSF does not contain relevant amounts of macromolecules or paramagnetic ions and the magnetic properties of CSF are largely unaffected by most neurological disorders³¹.

We found that both diffuse and focal WM abnormalities affected the WM-based calibration. On one hand, focal lesions led to a slight underestimation of PD values. On the other hand, diffuse WM damage might also impact the calibration resulting in slight PD differences (~ 0.1 – 0.2 p.u) between NAWM and WM while there was no difference in effective PD or when using CSF as reference. In such a ROI analysis, the impact from WM lesions may be occulted by the relative volume difference to whole white matter across patients. However, at the single subject level, their effect may be amplified. Therefore, we recalibrated PD as 100% in CSF, so that inter-subject variability in CSF would be negligible²⁷. To ensure that calibration is only based on voxels containing CSF and to avoid partial volume effects, we excluded voxels with T1 lower than 4s from the ventricle masks, which is an appropriate threshold given that the model estimated T1 of free water in brain tissue is 3.7 s³². Although T1 of CSF is known to be independent of field strength³³, reported values in literature show some variability ranging from 4 to 5 s. The CoV of the scaling factor did not vary substantially between the usage of different T1 cut-offs from 3 to 5 s. It was dramatically lower using CSF (0.74% vs. 37.79%). We effectively scale all voxels based on the assumption that CSF has the highest water fraction. One could either assume that the highest water fractions might be capped by the maximum intensity measured by the scanner or that biological variability in CSF is of lower order of magnitude.

Inter-subject variability is higher than in a previous study which used the conventional WM-based calibration, while intra-subject CoV is in the same order of magnitude¹². However, our current sample has a wider age range (42.1 ± 14.1 vs. 35 ± 7 y) than the study by Cooper and colleagues. Given the variability of ventricles sizes, the resulting inter-subject CoV is higher compared to normalization to a larger homogeneous WM region. Nonetheless, taking into consideration the variation in ventricular volume in the linear models, both linear association of PD with age and CoV remained similar whether we used the ventricles mask or a fixed set of 100 voxels within it. Although correlation exists between ventricular volume and age, as well as between ventricular volume and scaling factor, the scaling factor was not correlated to age. This means that although age variability in ventricular volume introduces variability in the PD scaling factor, the resulting inter-subject variability remains low compared to inter-subject variability from WM. An alternative approach would be to obtain a scaling factor with the use of an external reference such as a phantom to benefit from a stable and homogeneous volume³⁴. However, due to a lack of practicality, it is hardly considered for use in a clinical setting.

Finally, PD quantification methods may differ on the determination of the receiver sensitivity profile and values reported here are standardized for the method of quantitative B1 mapping³⁵. Volz et al. pointed out that physiological bias might be smoothed out and recommended to proceed carefully in the presence of pathology which may cause segmentation algorithms to fail or wherein the relationship between T1 and effective PD may be locally distorted⁴.

Age-related effects

We observed a non-linear age dependency of MT, R1 and R2* across various ROIs. Age effects could be best modelled linearly for PD and we found arguably a reduced impact of non-linear effects between 20 and 55y

Parameter (a.u)	ROI		Coefficient β	Confidence Interval (95%)	P-value	Adjusted P-value	Permutation P-value	Bootstrapped confidence intervals	
MT (%)	WM	Selected model: linear spline (F = 26.18, $p < 0.001$)						< 0.001	
		Intercept	1.085	(0.911, 1.261)	< 0.001	< 0.001	0.888	(0.867, 1.23)	
		Age (slope before 55)	-0.022	(-0.056, 0.011)	0.184	0.198	0.209	(-0.05, 0.006)	
		Age (slope after 55)	-0.154	(-0.2, -0.109)	< 0.001	< 0.001	< 0.001	(-0.186, -0.074)	
		Normalized ROI Volume	2.944	(1.958, 3.932)	< 0.001	< 0.001	0.013	(2.06, 4.15)	
	CGM	Selected model: quadratic fit (F = 5.43, $p = 0.006$)						0.019	
		Intercept	0.846	(0.842, 0.852)	< 0.001	< 0.001	< 0.001	(0.722, 1.005)	
		Age	-0.030	(-0.071, 0.011)	0.148	0.443	0.129	(-0.105, 0.038)	
		Age ²	-0.060	(-0.101, -0.02)	0.004	0.013	0.009	(-0.091, -0.018)	
	Thalamus	Selected model: quadratic fit (F = 6.47, $p < 0.001$)						0.046	
		Intercept	1.011	(0.881, 1.142)	< 0.001	< 0.001	0.109	(0.877, 1.14)	
		Normalized ROI Volume	36.549	(10.827, 62.272)	0.006	0.012	0.904	(10.83, 62.44)	
Age		-0.013	(-0.113, 0.088)	0.802	0.884	0.789	(-0.115, 0.105)		
Age ²		-0.130	(-0.223, -0.038)	0.006	0.012	0.005	(-0.218, -0.009)		
PD (%)	WM	Selected model: linear fit (F = 8.02, $p < 0.001$)						0.011	
		Intercept	76.119	(70.539, 81.701)	< 0.001	< 0.001	0.003	(73.53, 82.09)	
		Age	0.033	(0.014, 0.054)	0.002	0.004	0.002	(0.013, 0.052)	
		Normalized ROI Volume	-46.328	(-77.616, -5.041)	0.004	0.006	< 0.001	(-70.40, -23.42)	
R1 (s ⁻¹)	WM	Selected model: quadratic fit (F = 15.39, $p < 0.001$)						0.001	
		Intercept	0.659	(0.548, 0.771)	< 0.001	< 0.001	0.739	(0.535, 0.754)	
		Normalized ROI Volume	1.452	(0.839, 2.064)	< 0.001	< 0.001	0.293	(0.927, 2.119)	
		Age	-0.081	(-0.127, -0.034)	< 0.001	0.001	< 0.001	(-0.134, -0.029)	
		Age ²	-0.068	(-0.115, -0.021)	0.005	0.007	0.007	(-0.112, -0.021)	
	CGM	Selected model: quadratic fit (F = 4.95, $p = 0.01$)						0.04	
		Intercept	0.610	(0.608, 0.614)	< 0.001	< 0.001	0.896	(0.559, 0.692)	
		Age	0.005	(-0.019, 0.029)	0.657	0.898	0.861	(-0.033, 0.037)	
		Age ²	-0.036	(-0.06, -0.014)	0.003	0.009	0.002	(-0.059, -0.016)	
	Thalamus	Selected model: quadratic fit (F = 3.72, $p = 0.015$)						0.047	
		Intercept	0.667	(0.599, 0.737)	< 0.001	< 0.001	0.148	(0.599, 0.743)	
		Age	0.008	(-0.045, 0.061)	0.760	0.760	0.681	(-0.035, 0.062)	
		Age ²	-0.063	(-0.111, -0.016)	0.010	0.021	0.01	(-0.104, -0.015)	
		Normalized ROI Volume	12.691	(-0.945, 26.327)	0.068	0.175	0.798	(-1.656, 26.087)	
	Hippocampus	Selected model: quadratic fit (F = 3.56, $p = 0.018$)						0.016	
		Intercept	0.597	(0.571, 0.625)	< 0.001	< 0.001	0.001	(0.568, 0.626)	
		Age	0.034	(0.002, 0.067)	0.038	0.064	0.050	(0.007, 0.065)	
		Age ²	-0.040	(-0.072, -0.008)	0.016	0.039	0.014	(-0.063, -0.014)	
		Normalized Volume	-8.598	(-18.576, 1.381)	0.090	0.113	0.006	(-19.131, 2.65)	
		Sex: F vs M	-0.007	(-0.016, 0.003)	0.170	0.170	0.175	(-0.0162, 0.003)	
R2* (s ⁻¹)	WM	Selected model: linear spline (F = 6.50, $p < 0.001$)						0.052	
		Intercept	17.314	(14.905, 19.723)	< 0.001	< 0.001	0.155	(14.851, 19.258)	
		Age (slope before 55)	0.252	(-0.22, 0.724)	0.290	0.395	0.385	(-0.226, 0.682)	
		Age (slope after 55)	-0.648	(-1.22, -0.077)	0.027	0.035	0.026	(-1.00, -0.043)	
		Normalized Volume	20.286	(6.687, 33.885)	0.004	0.007	0.902	(9.216, 34.11)	
	CGM	Selected model: quadratic fit (F = 10.17, $p < 0.001$)						0.005	
		Intercept	16.796	(16.687, 16.905)	< 0.001	< 0.001	1	(14.92, 20.98)	
		Age	1.127	(0.199, 2.056)	0.018	0.018	0.153	(-0.853, 2.199)	
		Age ²	-1.772	(-2.702, -0.844)	< 0.001	< 0.001	< 0.001	(-2.674, -0.743)	

Table 3. MPM selected models in white matter (WM), cortical grey matter (CGM), thalamus and hippocampus. Normalized ROI volume was calculated as ROI volume divided by total intra-cranial volume. Age coefficients estimates are given in respective parameter unit per year (a.u/y). Empirical permutation p -values from permutation testing (1000 iterations) are given for the model and each term. 95% confidence intervals of the model coefficients are given for each model term from bootstrapped distributions (1000 iterations). The significant age-related effects hold after permutation testing or bootstrap.

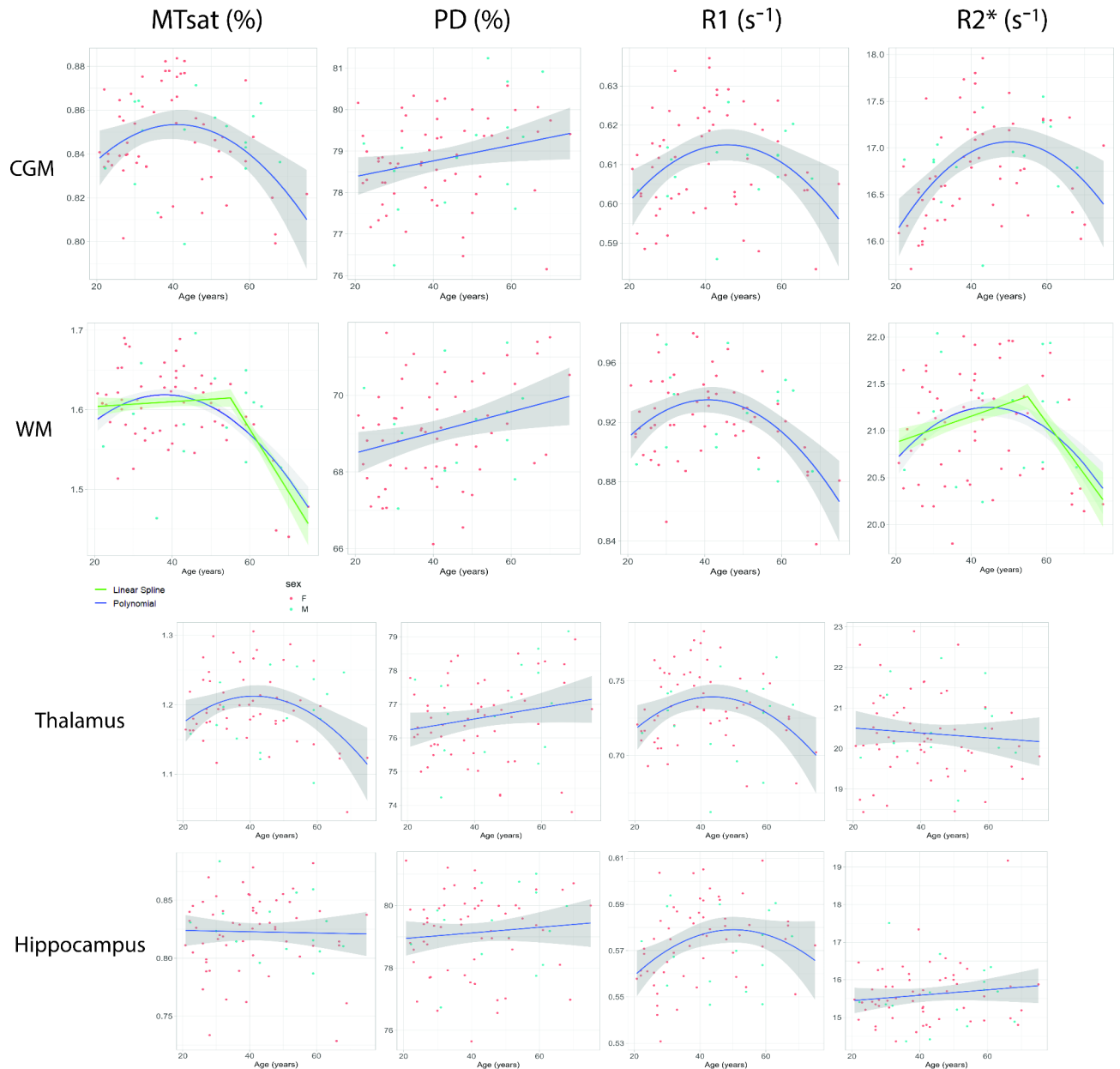


Fig. 5. Scatterplots and fitted trajectories (blue) for the described ROIs. Green curve shows the linear spline with a cut-off of 55y when it performed better than the other models. Red and green dots represent women and men respectively.

for both MT and $R2^*$ in WM. Our findings corroborate MPM studies on brain aging which reported negative correlation between age and MT across the cortex along positive correlations between age and $R2^*$ in the basal ganglia^{9–11,36}.

A quadratic model provided an accurate representation of the non-linear relationship between MT and age, illustrating the U-shaped pattern in myelination over lifespan, consistent with myelin-driven changes in volume and MRI contrast across the cortex³⁷. Quantitative R1 has also shown a quadratic trajectory against age indicative of region-specific myelin maturation stabilizing into middle age followed by degeneration³⁸. Interestingly, we noticed a concurrence between R1, MT and $R2^*$ in WM and CGM owing to their sensitivity to macromolecular, myelin, iron and water content³⁹.

Except for its linear increase in WM, we did not find any age-related association to PD in the investigated ROIs. Across the cortex, this is consistent with Seiler et al.⁴⁰ who reported that global cortical PD did not show a significant correlation with age. Overall, PD as a surrogate for water may be less sensitive to age-related changes of tissues. However, a limited sample size and values extracted from a single ROI do not allow generalization of the results to the whole cortex because of regional heterogeneity.

Linear and polynomial fits of $R2^*$ versus age performed significantly better on our data across ROIs than exponential saturation functions as the latter could not keep up with the increase in $R2^*$ and its variability in our older participants. Given our limited sample size, dependency of $R2^*$ on age across ROIs may not follow the putative steep iron increase from early childhood to adulthood, as shown by global cubic fits for the caudate, putamen, and globus pallidus reported in another study⁴¹. Pallidal calcification was often seen in our older healthy participants, which we considered as a normal aging phenomenon contributing to the $R2^*$ inter-subject variability in the basal ganglia as hyperintensities may originate from the presence of minerals such as calcium and zinc especially around the globus pallidus⁴². Finally, increased variability with age in $R2^*$ may partly be explained by noisier measurements given the sensitivity to motion inherent to the multi-echo FLASH acquisition. As shown by the correlation between age and motion degradation index, motion may also be a predictor as the ability to remain still in the scanner may worsen with age. Specifically, head motion extends to the noise level of relaxometry estimates derived from the raw echoes quantified by the variability of $R2^*$ in WM⁴³.

Comparison of MPM measurements

We characterized WM, CGM, DGM brain tissue classes in healthy subjects and compared WM and WML across MS patients and healthy participants. Absolute deviations in mean or median between our HC MPM values across ROIs and those reported in literature were in the same range as differences between previous studies highlighting the reproducibility of quantitative MPM^{6,7,44}.

Distributions of MPM-derived measures across WM, CGM and DGM regions reflect local iron concentration and myelination levels. WM generally has lower PD than both types of grey matter because of its high myelin content, which displaces protons, while CGM exhibits lower myelination⁴⁵. Conversely, MT values are higher in WM and lower in CGM, whereas DGM nuclei typically display MT that vary based on regional myelin content and iron accumulation⁴⁶. R1 values are highest in WM due to the high myelin concentration, shortening the longitudinal relaxation time and lower in CGM, while in DGM, R1 may be influenced by elevated iron content, particularly in regions like the basal ganglia³⁹. Generally, $R2^*$ values tend to be higher in DGM due to iron-rich areas like the basal ganglia¹¹, and in WM pathways, where $R2^*$ increases with myelination and iron accumulation, with lower levels in CGM. Indeed, tissue areas rich in iron often co-localize with regions of elevated myelin content⁴⁷, given the role of iron in myelin synthesis and homeostasis, or the high iron concentration within glial cells⁴⁸, adding to the dependence of $R2^*$ on the orientation of WM fibers with respect to the magnetic field⁴⁹.

In HC, T2w WMH had increased PD and reduced MT, R1 and $R2^*$ compared to WM. WML of MS patients show increased PD and reduced MT, R1 and $R2^*$ compared to MS-NAWM, HC-WM and HC-WML. NAWM of MS patients showed increased PD and decreased MT, R1 and $R2^*$ compared to HC-WM. This demonstrates that MPM may detect pronounced focal damage and structural loss while it is also sensitive to diffuse white matter pathology, as NAWM which appears unaffected on conventional MRI can be differentiated from healthy WM^{44,50}. In particular, demyelination, axonal degeneration, inflammation, gliosis and edema are exacerbated in MS plaques resulting in higher discrepancy in MPM values from WM and WML of healthy controls, corroborating findings from other studies using quantitative relaxometry, MT imaging, and diffusion MRI⁵¹. However, MS lesions are heterogeneous and present varying degrees of degeneration, de/re-myelination and inflammation, thus discriminating specific lesion types remains to be explored^{52,53}.

Implications for clinical research in multiple sclerosis

Strengths of this study include using manufacturer sequences, which allow ready implementation on standard scanners. In consideration of future research implicating WM lesions and abnormalities in multiple sclerosis and related disorders, we included them in the general pipeline for lesion-filling and to improve PD quantification, as (i) the presence of lesions or enlarged ventricles may cause segmentation to fail and (ii) global effects observed in WM might transfer to lesion-specific localized effects, (iii) the pipeline could be translated to demyelinating diseases like neuromyelitis optica spectrum disorders presenting a very similar characterization of lesions with overlapping clinical features⁵⁴. Since the prevalence and severity of non-specific T2w WMH tend to rise with age with a majority of non-demented people aged above 60 exhibiting cerebral lesions⁵⁵, future studies using MPM could aim at further differentiating MS-WML from HC-WML. As proof of principle, given the limited sample size of MS patients, we only explored associations between MPM-derived measurements and the clinical variables described. Clinical disability reflected in EDSS, T2 lesion volume or disease duration is likely to cause changes in brain tissue properties measured by quantitative MRI. Both diffuse and focal alterations seem to contribute to disability in MS, as we observed significant associations between these clinical variables and MPM-derived measures in both NAWM and WML of MS patients. This underscores the potential of quantitative maps as imaging biomarkers for disease progression, however further interpretation warrants future clinical applications in a larger cohort and longitudinal studies to establish the predictive value of MPM for clinical outcomes.

Lastly, we hypothesized that MPM measurements might demonstrate more consistency in younger healthy individuals while displaying greater variability in older populations to acknowledge the impact of pre-clinical degeneration. Biological age may contribute most to the inter-subject variability and even be the strongest predictor for pathophysiological changes. Seminal studies have reported early and late nonlinear age-dependence in the lifespan trajectories of quantitative parameters, with distinct patterns in MT mimicking the inverted U-shaped trajectory of human brain myelination³⁷ and in $R2^*$ analogous to the exponential cerebral increase of non-heme iron⁵⁶. Yet, this relationship may be altered in disease. In multi-center or randomized clinical trials, due to discrepancy in age distribution of unmatched cohorts, including age as a linear predictor may be inadequate if one aims to fully capture the true age-related variability when manipulating biomarkers. It may be recommended to check and correct for non-linear age effects by fitting the response with age as an independent parameter. For example, after fitting with an exponential saturation function, Ropele et al. assessed inter-subject

and inter-scanner variability of $R2^*$ and attributed large $R2^*$ variations to age suggestive of iron accumulation while scanner differences had a low impact⁵⁷.

Limitations

Although significant age-related effects hold after bootstrap and permutation testing, our current healthy control sample primarily includes 77 late adulthood individuals, with fewer participants over 60 years old, which may be the main cause of the observed non-linear patterns. Furthermore, we included a limited number of MS patients with WM abnormalities. Even though the sample size is small for robust non-linear models of age-related effects, we report healthy population MPM data which can serve as control data and such studies are scarce given the novelty of the protocol. Longitudinal studies are however superior to assess chronological pathological changes and reduce bias due to the large interindividual variability. Another liability is that the age and sex distributions of the recruited participants resemble those of typical cohorts of autoimmune neuroinflammatory diseases with a strong preponderance of women, what may drive the absence of sex differences in MPM-derived parameters between men and women observed in our study. This may however become a strength when studying such clinical populations. Indeed, our pipeline considered the inclusion of WML with MPM and is readily available for upcoming research in diseases like multiple sclerosis. Consequently, the recruited population did not permit to have a good representation of early and late developmental changes occurring in the brain to effectively explore the impact of aging on quantitative maps and associate it to decline in cognition or motor function. Moreover, this study was done on a white population, so our results are not necessarily applicable to other ethnicities. In this study, no visual rating of the WML was attempted as they mostly served to establish the pipeline and will be further discussed and investigated in a following study to discriminate MS specific lesions from the WM lesions described in healthy participants which are likely microangiopathic. Future developments should target improvements in both sensitivity and specificity of MRI biomarkers, as well as clinical applicability with regards to disease models.

Conclusion

In conclusion, we present a fast quantitative MPM pipeline at 1.6 mm isotropic resolution, which can be readily used in a clinical protocol based on manufacturer sequences, along post-processing methods including standardization of PD maps and healthy brain data acquired with it. The protocol is anticipated to possess a higher sensitivity in identifying pathological alterations in future applications in MS¹² and to provide insight into both visible lesions and subtle changes in white matter. Importantly, previous studies^{6,7}, as well as the current study provide essential reference values and contribute datasets to assist clinical researchers in conducting thorough power analyses and report effect sizes that carry significance for future investigations in the context of clinical studies.

Data availability

The analysis pipeline is available at <https://clinicalmpm.github.io/>, including the sequence configuration for Siemens PRISMA scanners. MRI data from this study cannot be shared publicly due to constraints from the European General Data Protection Regulation and its implementation into German laws and required consent from participants.

Received: 7 October 2024; Accepted: 18 November 2024

Published online: 16 December 2024

References

- Weiskopf, N., Edwards, L. J., Helms, G., Mohammadi, S. & Kirilina, E. Quantitative magnetic resonance imaging of brain anatomy and in vivo histology. *Nat. Rev. Phys.* **3**, 570–588. <https://doi.org/10.1038/s42254-021-00326-1> (2021).
- Cercignani, M., Dowell, N. G. & Tofts, P. S. *Quantitative MRI of the brain: Principles of physical measurement*. (2018).
- Gelman, N., Ewing, J. R., Gorell, J. M., Spickler, E. M. & Solomon, E. G. Interregional variation of longitudinal relaxation rates in human brain at 3.0 T: Relation to estimated iron and water contents. *Magn. Reson. Med.* **45**, 71–79. [https://doi.org/10.1002/1522-2594\(200101\)45:1%3c71::aid-mrm1011%3e3.0.co;2-2](https://doi.org/10.1002/1522-2594(200101)45:1%3c71::aid-mrm1011%3e3.0.co;2-2) (2001).
- Schmierer, K. et al. Quantitative magnetization transfer imaging in postmortem multiple sclerosis brain. *J. Magn. Reson. Imaging* **26**, 41–51. <https://doi.org/10.1002/jmri.20984> (2007).
- Langkammer, C. et al. Quantitative MR imaging of brain iron: A postmortem validation study. *Radiology* **257**, 455–462. <https://doi.org/10.1148/radiol.10100495> (2010).
- Weiskopf, N. et al. Quantitative multi-parameter mapping of $R1$, PD^* , MT , and $R2^*$ at 3T: A multi-center validation. *Front. Neurosci.* **7**, 95. <https://doi.org/10.3389/fnins.2013.00095> (2013).
- Leutritz, T. et al. Multiparameter mapping of relaxation ($R1$, $R2^*$), proton density and magnetization transfer saturation at 3 T: A multicenter dual-vendor reproducibility and repeatability study. *Hum. Brain Mapp.* **41**, 4232–4247. <https://doi.org/10.1002/hbm.25122> (2020).
- Tabelow, K. et al. hMRI - A toolbox for quantitative MRI in neuroscience and clinical research. *Neuroimage* **194**, 191–210. <https://doi.org/10.1016/j.neuroimage.2019.01.029> (2019).
- Taubert, M. et al. Converging patterns of aging-associated brain volume loss and tissue microstructure differences. *Neurobiol. Aging* **88**, 108–118. <https://doi.org/10.1016/j.neurobiolaging.2020.01.006> (2020).
- Draganski, B. et al. Regional specificity of MRI contrast parameter changes in normal ageing revealed by voxel-based quantification (VBQ). *Neuroimage* **55**, 1423–1434. <https://doi.org/10.1016/j.neuroimage.2011.01.052> (2011).
- Callaghan, M. F. et al. Widespread age-related differences in the human brain microstructure revealed by quantitative magnetic resonance imaging. *Neurobiol. Aging* **35**, 1862–1872. <https://doi.org/10.1016/j.neurobiolaging.2014.02.008> (2014).
- Cooper, G. et al. Quantitative multi-parameter mapping optimized for the clinical routine. *Front. Neurosci.* **14**, 611194. <https://doi.org/10.3389/fnins.2020.611194> (2020).
- Harbo, H. F., Gold, R. & Tintore, M. Sex and gender issues in multiple sclerosis. *Ther. Adv. Neurol. Disord.* **6**, 237–248. <https://doi.org/10.1177/1756285613488434> (2013).

14. Volz, S. et al. Quantitative proton density mapping: Correcting the receiver sensitivity bias via pseudo proton densities. *Neuroimage* **63**, 540–552. <https://doi.org/10.1016/j.neuroimage.2012.06.076> (2012).
15. Sperber, P. S. et al. Berlin registry of neuroimmunological entities (BERLimmun): Protocol of a prospective observational study. *BMC Neurol.* **22**, 479. <https://doi.org/10.1186/s12883-022-02986-7> (2022).
16. Heine, J. et al. Structural brain changes in patients with post-COVID fatigue: A prospective observational study. *EClinicalMedicine* **58**, 101874. <https://doi.org/10.1016/j.eclinm.2023.101874> (2023).
17. Schliesseit, J., Oertel, F. C., Cooper, G., Brandt, A. U. & Bellmann-Strobl, J. Longitudinal analysis of primary and secondary factors related to fatigue in multiple sclerosis. *Acta Neurol. Belg.* **121**, 271–274. <https://doi.org/10.1007/s13760-020-01545-6> (2021).
18. Thompson, A. J. et al. Diagnosis of multiple sclerosis: 2017 revisions of the McDonald criteria. *Lancet Neurol* **17**, 162–173. [https://doi.org/10.1016/S1474-4422\(17\)30470-2](https://doi.org/10.1016/S1474-4422(17)30470-2) (2018).
19. Helms, G., Dathe, H. & Dechent, P. Quantitative FLASH MRI at 3T using a rational approximation of the Ernst equation. *Magn. Reson. Med.* **59**, 667–672. <https://doi.org/10.1002/mrm.21542> (2008).
20. Kellner, E., Dhital, B., Kiselev, V. G. & Reiser, M. Gibbs-ringing artifact removal based on local subvoxel-shifts. *Magn. Reson. Med.* **76**, 1574–1581. <https://doi.org/10.1002/mrm.26054> (2016).
21. Lutti, A. et al. Restoring statistical validity in group analyses of motion-corrupted MRI data. *Hum. Brain Mapp.* **43**, 1973–1983. <https://doi.org/10.1002/hbm.25767> (2022).
22. Tustison, N. J. et al. N4ITK: Improved N3 bias correction. *IEEE Trans. Med. Imaging* **29**, 1310–1320. <https://doi.org/10.1109/TMI.2010.2046908> (2010).
23. Chien, C. et al. Prediction of high and low disease activity in early MS patients using multiple kernel learning identifies importance of lateral ventricle intensity. *Mult. Scler. J. Exp. Transl. Clin.* **8**, 20552173221109770. <https://doi.org/10.1177/20552173221109770> (2022).
24. Fazekas, F., Chawluk, J. B., Alavi, A., Hurtig, H. I. & Zimmerman, R. A. MR signal abnormalities at 1.5 T in Alzheimer's dementia and normal aging. *AJR Am. J. Roentgenol.* **149**, 351–356. <https://doi.org/10.2214/ajr.149.2.351> (1987).
25. van Straaten, E. C. et al. Impact of white matter hyperintensities scoring method on correlations with clinical data: The LADIS study. *Stroke* **37**, 836–840. <https://doi.org/10.1161/01.STR.0000202585.26325.74> (2006).
26. Henschel, L. et al. FastSurfer—A fast and accurate deep learning based neuroimaging pipeline. *Neuroimage* **219**, 117012. <https://doi.org/10.1016/j.neuroimage.2020.117012> (2020).
27. Mezer, A. et al. Quantifying the local tissue volume and composition in individual brains with magnetic resonance imaging. *Nat. Med.* **19**, 1667–1672. <https://doi.org/10.1038/nm.3390> (2013).
28. Desikan, R. S. et al. An automated labeling system for subdividing the human cerebral cortex on MRI scans into gyral based regions of interest. *Neuroimage* **31**, 968–980. <https://doi.org/10.1016/j.neuroimage.2006.01.021> (2006).
29. Kurtzke, J. F. Rating neurologic impairment in multiple sclerosis: An expanded disability status scale (EDSS). *Neurology* **33**, 1444–1452. <https://doi.org/10.1212/wnl.33.11.1444> (1983).
30. Sexton, C. E. et al. Accelerated changes in white matter microstructure during aging: A longitudinal diffusion tensor imaging study. *J. Neurosci.* **34**, 15425–15436. <https://doi.org/10.1523/JNEUROSCI.0203-14.2014> (2014).
31. Hegen, H., Auer, M., Zeileis, A. & Deisenhammer, F. Upper reference limits for cerebrospinal fluid total protein and albumin quotient based on a large cohort of control patients: Implications for increased clinical specificity. *Clin. Chem. Lab. Med.* **54**, 285–292. <https://doi.org/10.1515/cclm-2015-0253> (2016).
32. Callaghan, M. F., Helms, G., Lutti, A., Mohammadi, S. & Weiskopf, N. A general linear relaxometry model of R1 using imaging data. *Magn. Reson. Med.* **73**, 1309–1314. <https://doi.org/10.1002/mrm.25210> (2015).
33. Rooney, W. D. et al. Magnetic field and tissue dependencies of human brain longitudinal $1H_2O$ relaxation in vivo. *Magn. Reson. Med.* **57**, 308–318. <https://doi.org/10.1002/mrm.21122> (2007).
34. Lorio, S. et al. Flexible proton density (PD) mapping using multi-contrast variable flip angle (VFA) data. *Neuroimage* **186**, 464–475. <https://doi.org/10.1016/j.neuroimage.2018.11.023> (2019).
35. Weiskopf, N. et al. Unified segmentation based correction of R1 brain maps for RF transmit field inhomogeneities (UNICORT). *Neuroimage* **54**, 2116–2124. <https://doi.org/10.1016/j.neuroimage.2010.10.023> (2011).
36. Carey, D. et al. Quantitative MRI provides markers of intra-, inter-regional, and age-related differences in young adult cortical microstructure. *Neuroimage* **182**, 429–440. <https://doi.org/10.1016/j.neuroimage.2017.11.066> (2018).
37. Bartzokis, G. et al. Multimodal magnetic resonance imaging assessment of white matter aging trajectories over the lifespan of healthy individuals. *Biol. Psychiatry* **72**, 1026–1034. <https://doi.org/10.1016/j.biopsych.2012.07.010> (2012).
38. Yeatman, J. D., Wandell, B. A. & Mezer, A. A. Lifespan maturation and degeneration of human brain white matter. *Nat. Commun.* **5**, 4932. <https://doi.org/10.1038/ncomms5932> (2014).
39. Stuber, C. et al. Myelin and iron concentration in the human brain: A quantitative study of MRI contrast. *Neuroimage* **93**(Pt 1), 95–106. <https://doi.org/10.1016/j.neuroimage.2014.02.026> (2014).
40. Seiler, A. et al. Multiparametric quantitative MRI in neurological diseases. *Front. Neurol.* **12**, 640239. <https://doi.org/10.3389/fneur.2021.640239> (2021).
41. Treit, S. et al. R2* and quantitative susceptibility mapping in deep gray matter of 498 healthy controls from 5 to 90 years. *Hum. Brain Mapp.* **42**, 4597–4610. <https://doi.org/10.1002/hbm.25569> (2021).
42. Acosta-Cabronero, J., Betts, M. J., Cardenas-Blanco, A., Yang, S. & Nestor, P. J. In Vivo MRI mapping of brain iron deposition across the adult lifespan. *J. Neurosci.* **36**, 364–374. <https://doi.org/10.1523/JNEUROSCI.1907-15.2016> (2016).
43. Castella, R. et al. Controlling motion artefact levels in MR images by suspending data acquisition during periods of head motion. *Magn. Reson. Med.* **80**, 2415–2426. <https://doi.org/10.1002/mrm.27214> (2018).
44. Lommers, E. et al. Multiparameter MRI quantification of microstructural tissue alterations in multiple sclerosis. *Neuroimage Clin.* **23**, 101879. <https://doi.org/10.1016/j.nicl.2019.101879> (2019).
45. Tofts, P. S. In *Quantitative MRI of the Brain* 83–109 (2003).
46. Sled, J. G. et al. Regional variations in normal brain shown by quantitative magnetization transfer imaging. *Magn. Reson. Med.* **51**, 299–303. <https://doi.org/10.1002/mrm.10701> (2004).
47. Fukunaga, M. et al. Layer-specific variation of iron content in cerebral cortex as a source of MRI contrast. *Proc. Natl. Acad. Sci. U. S. A.* **107**, 3834–3839. <https://doi.org/10.1073/pnas.0911177107> (2010).
48. Ward, R. J., Zucca, F. A., Duyn, J. H., Crichton, R. R. & Zecca, L. The role of iron in brain ageing and neurodegenerative disorders. *Lancet Neurol.* **13**, 1045–1060. [https://doi.org/10.1016/S1474-4422\(14\)70117-6](https://doi.org/10.1016/S1474-4422(14)70117-6) (2014).
49. Bender, B. & Klose, U. The in vivo influence of white matter fiber orientation towards B(0) on T2* in the human brain. *NMR Biomed.* **23**, 1071–1076. <https://doi.org/10.1002/nbm.1534> (2010).
50. De Stefano, N. et al. Diffuse axonal and tissue injury in patients with multiple sclerosis with low cerebral lesion load and no disability. *Arch. Neurol.* **59**, 1565–1571. <https://doi.org/10.1001/archneur.59.10.1565> (2002).
51. Cairns, J. et al. Diffusely abnormal white matter in multiple sclerosis. *J. Neuroimaging* **32**, 5–16. <https://doi.org/10.1111/jon.12945> (2022).
52. Rahmanzadeh, R. et al. A new advanced MRI biomarker for remyelinated lesions in multiple sclerosis. *Ann. Neurol.* **92**, 486–502. <https://doi.org/10.1002/ana.26441> (2022).
53. Galbusera, R. et al. Postmortem quantitative MRI disentangles histological lesion types in multiple sclerosis. *Brain Pathol.* **33**, e13136. <https://doi.org/10.1111/bpa.13136> (2023).

54. Gerales, R. et al. The current role of MRI in differentiating multiple sclerosis from its imaging mimics. *Nat. Rev. Neurol.* **14**, 213. <https://doi.org/10.1038/nrneurol.2018.39> (2018).
55. de Leeuw, F. E. et al. Hypertension and cerebral white matter lesions in a prospective cohort study. *Brain* **125**, 765–772. <https://doi.org/10.1093/brain/awf077> (2002).
56. Hallgren, B. & Sourander, P. The effect of age on the non-haemin iron in the human brain. *J. Neurochem.* **3**, 41–51. <https://doi.org/10.1111/j.1471-4159.1958.tb12607.x> (1958).
57. Ropele, S. et al. Multicenter R2* mapping in the healthy brain. *Magn. Reson. Med.* **71**, 1103–1107. <https://doi.org/10.1002/mrm.24772> (2014).
58. Lublin, F. D. et al. Defining the clinical course of multiple sclerosis: The 2013 revisions. *Neurology* **83**, 278–286. <https://doi.org/10.1212/WNL.0000000000000560> (2014).

Acknowledgements

This work was supported by the Berlin Center for Advanced Neuroimaging, by iNAMES—MDC—Weizmann—Helmholtz International Research School for Imaging and Data Science from NANO to MESO, the German Research Foundation (DFG) and the Open Access Publication Fund of Charité-Universitätsmedizin Berlin. For the studies ViMS and BERLIMMUN, we acknowledge institutional support by NCRC—Neuroscience Clinical Research Center funded by the Deutsche Forschungsgemeinschaft (DFG, German Research Foundation) under Germany's Excellence Strategy—EXC-2049–390688087 and Charité-BIH. We are thankful to our MR technicians, Cynthia Kraut and Susan Pikol, for their assistance in data acquisition.

Author contributions

Data analysis: H.T, Q.C Data curation: H.T, Q.C., C.F, T.S.H, P.S, R.R, S.A, C.C Conceptualization and Supervision: F.P, A.U.B Methodology: S.H, H.T Review and editing: Q.C., C.F, T.H, T.S.H, P.S, L.A, C.C, M.S, S.H, D.M, F.P, A.U.B Writing—original draft: H.T, T.H

Funding

Open Access funding enabled and organized by Projekt DEAL.

Declarations

Competing interests

H.T is supported by iNAMES—MDC—Weizmann—Helmholtz International Research School for Imaging and Data Science from NANO to MESO. Q.C is supported by the Chinese Scholarship Council (CSC). C.C has received research support from Novartis and Alexion and is a part of a consortium funded by the U.S. Department of Defense, unrelated to this study. She also serves as a member of the Standing Committee on Science for the Canadian Institutes of Health Research (CIHR). D.M has received a research scholarship from the Berlin Institute of Health at Charité, Berlin, Germany. S.A received speaker's honoraria from Bayer, Alexion, Roche and research grants from Stiftung Charité, Fritz-Thyssen-Stiftung, HEAD Genuit Stiftung, Rahel Hirsch Program, Novartis and Roche, all unrelated to this study. R.R. received speaking honoraria from Roche unrelated to this study. M.S. has received consulting fees from Roche, Pliant therapeutics, and Octave Bioscience all unrelated to this study. He is named as inventor on a patent describing use of N-acetylglucosamine as myelination and immunomodulating therapy. T.S.H has received research funding from Celgene/bms and speaker honoraria from AbbVie, Bayer, and Roche both unrelated to this work. A.U.B is cofounder and holds shares of medical technology companies Motognosis GmbH and Nocturne GmbH. He is named as inventor on several patents and patent applications describing methods for retinal image analyses, motor function analysis, multiple sclerosis serum biomarkers and myelination therapies utilizing N-glycosylation modification. He is cofounder of IMSVISUAL and has served as member of the board of directors and secretary/treasurer of IMSVISUAL. AUB is now full-time employee and holds stocks and stock options of Eli Lilly and Company. His contribution to this work is his own and does not represent a contribution from Eli Lilly. F.P. has received research funding from Biogen, Genzyme, Guthy Jackson Foundation, Merck, Serono, Novartis, Bayer and Roche all unrelated to this work. He has received consulting fees from Alexion, Roche, Horizon, Neuraxpharm and speaker honoraria from Almirall, Bayer, Biogen, GlaxoSmithKline, Hexal, Merck, Sanofi, Genzyme, Novartis, Viela Bio, UCB, Mitsubishi Tanabe, Celgene, Guthy Jackson Foundation, Serono and Roche all unrelated to this study.

Additional information

Supplementary Information The online version contains supplementary material available at <https://doi.org/10.1038/s41598-024-80274-9>.

Correspondence and requests for materials should be addressed to C.F. or F.P.

Reprints and permissions information is available at www.nature.com/reprints.

Publisher's note Springer Nature remains neutral with regard to jurisdictional claims in published maps and institutional affiliations.

Open Access This article is licensed under a Creative Commons Attribution 4.0 International License, which permits use, sharing, adaptation, distribution and reproduction in any medium or format, as long as you give appropriate credit to the original author(s) and the source, provide a link to the Creative Commons licence, and indicate if changes were made. The images or other third party material in this article are included in the article's Creative Commons licence, unless indicated otherwise in a credit line to the material. If material is not included in the article's Creative Commons licence and your intended use is not permitted by statutory regulation or exceeds the permitted use, you will need to obtain permission directly from the copyright holder. To view a copy of this licence, visit <http://creativecommons.org/licenses/by/4.0/>.

© The Author(s) 2024